THE DYNAMICS OF Br FORMATION FROM THE PRIMARY AND SECONDARY C–Br BOND DISSOCIATION OF OXALYL BROMIDE NEAR 265 and 234 nm

D. Paul [1,2*], H. K. Kim [1], Md. Mostafizur Rahman [3], T. K. Kim [1,4]

[1] Department of Chemistry and Chemistry Institute for Functional Materials, Pusan National University, Busan 609-735, Korea
[2] Department of Chemistry, Bangabandhu Sheikh Mujibur Rahman Science and Technology University, Gopalganj-8100, Bangladesh; e-mail: pauldababrata@gmail.com
[3] Department of Chemistry, Shahjalal University of Science and Technology, Sylhet-3114, Bangladesh
[4] Department of Chemistry, Yonsei University, Korea

The photodissociation dynamics of oxalyl bromide is investigated near 265 and 234 nm using the velocity map ion imaging technique coupled with a state selective [2+1] resonance-enhanced multiphoton ionization scheme. The translational energy distribution and ^2P_J, J = 3/2, 1/2 parameters of the Br atom formation process are extracted from two-dimensional ion images. The trimodal energy distribution of Br($^2P_{3/2}$) atoms is attributed to the primary C–Br bond fission as well as the secondary dissociation of bromine-containing C_2O_2Br radicals produced from the primary Br and Br pathways. The conclusions are confirmed by the recoil anisotropy and the distribution width corresponding to the individual components. The branching ratio Br($^2P_{3/2}$)/Br($^2P_{1/2}$) confirms the excitation energy dependence.*

Keywords: *photodissociation dynamics, oxalyl bromide, ion-imaging.*

ДИНАМИКА ОБРАЗОВАНИЯ БРОМА ПРИ ДИССОЦИАЦИИ ПЕРВИЧНОЙ И ВТОРИЧНОЙ СВЯЗИ C–Br ОКСАЛИЛБРОМИДА ВБЛИЗИ 265 и 234 нм

D. Paul [1,2*], H. K. Kim [1], Md. M. Rahman [3], T. K. Kim [1,4]

УДК 541.141.7

[1] Пусанский национальный университет, Пусан 609-735, Корея
[2] Научно-технический университет имени Шейха Муджибура Рахмана Бангабандху, Гопалгандж-8100, Бангладеш; e-mail: pauldababrata@gmail.com
[3] Шахджалальский университет науки и техники, Силхет-3114, Бангладеш
[4] Университет Йонсей, Корея

(Поступила 27 мая 2020)

Динамика фотодиссоциации оксалилбромида исследована вблизи 265 и 234 нм с помощью метода визуализации карты скоростей в сочетании с многофотонной ионизацией с селективным по состояниям [2+1] резонансным усилением. Распределение трансляционных энергетических уровней и параметры атома Br (^2P_J, J = 3/2, 1/2) извлекаются из двумерных изображений ионов. Тримодальное распределение энергии атомов Br ($^2P_{3/2}$) объясняется первичным расщеплением связи C–Br, а также вторичной диссоциацией бромсодержащих радикалов C_2O_2Br, образующихся из Br и Br на первичной стадии. Выводы подтверждаются анизотропией отдачи и шириной распределения, соответствующего отдельной компоненте. Отношение Br($^2P_{3/2}$)/Br($^2P_{1/2}$) свидетельствует о зависимости от энергии возбуждения.*

Ключевые слова: *динамика фотодиссоциации, оксалилбромид, ионная визуализация.*

Introduction. The UV photodissociation of CH_3X as the simplest alkyl halide system has been widely investigated in their *A*-band excitation both experimentally and theoretically [1–5]. The $\sigma^*\leftarrow n$ electronic transition localized on the C−X bond is responsible for the *A*-band photodissociation. Compared to the simple alkyl halide, an oxalyl halide ($C_2O_2X_2$) has two equivalent C−Br bonds with the π-electronic system that exerts $\pi^*\leftarrow n$ transition in the vicinity of the $\sigma^*\leftarrow n$ excitation. As a result, surface interactions among the (n,π^*) and (n,σ^*) states and the secondary dissociation of C−Br may interfere with formatting the X/X* pathways. The wavelength-dependent photodissociation dynamics of oxalyl chloride has been investigated [6–9]. At 235 nm, three fragments (fast Cl*/Cl, rotationally excited CO, and COCl radical) were formed from an impulsive three-body dissociation pathway with subsequent COCl radical decomposition to rotationally exciting CO and Cl, whereas, similar a two-step mechanism was also observed at 193 nm [7]. On the other hand, Wang et al. detected the rotationally-resolved emission of CO ($v \le 3$) at 248 nm using a step-scan time-resolved Fourier-transform spectrometer and suggested that the secondary dissociation of COCl occurs synchronously in its vibrational ground state [10]. Later, this observation was supported by the *ab initio* molecular dynamics simulations [11]. A Cl_2 elimination channel was also observed in one-photon dissociation of $(COCl)_2$ at 248 nm [12]. The relative quantum yield was 0.8±0.4 initiated from the $\tilde{X}\,^1A_g$ ground state surface $(COCl)_2$ via internal conversion.

In comparison with the $C_2O_2Cl_2$, the photodissociation dynamics of oxalyl bromide ($C_2O_2Br_2$) has received less attention even though its study gives an opportunity to unravel the effects due to the mass and spin-orbit coupling energy. Lin et al. studied the Br_2 molecular elimination of $C_2O_2Br_2$ at 248 nm using cavity ring-down absorption spectroscopy [13]. They proposed that the ground state $C_2O_2Br_2$ via internal conversion was responsible for the Br_2 elimination process with a 11% quantum yield. In a similar observation, the Br_2 molecular elimination of $C_2O_2Br_2$, at 435.8 and 265.2 nm was also proposed by Tuttle et al. based on their pressure and absorption dependent experiment [14]. Although a few studies on the photodissociation dynamics of $C_2O_2Br_2$ have been reported, no information on the Br/Br* formation dynamics has appeared yet. For this purpose, in the present study, the Br/Br* generating dynamics of $C_2O_2Br_2$ near 234 and 265 nm has been investigated. The velocity map ion-imaging (VMI) technique was used to obtain the spatial distributions of the nascent Br atoms. The [2+1] resonance-enhanced multiphoton ionization (REMPI) scheme was used for state-selective detections of Br($^2P_{3/2}$) and Br*($^2P_{1/2}$) generated after the photolysis of $C_2O_2Br_2$ at two different excitation wavelengths. The measured total translational energy distributions, recoil anisotropic parameters, and the relative quantum yields were used to explore photo-induced stepwise multi-body dissociation pathways.

Experimental setup. Imaging experiments were carried out on a VMI (charged particle analyzer) spectrometer constructed based on the Eppink and Parker design [15], which includes three electrodes, namely, a repeller, an extractor, and a ground. The ion-optics voltage setup and the position of the interaction region with respect to the repeller electrode were optimized with the SIMION simulation. The field ratio between the extractor and the repeller was 0.705. The optimized voltage combination on the repeller (V_1), extractor (V_2), and ground (V_3) form a weak converging electrostatic lens (Fig. 1a). The sample mixture was prepared

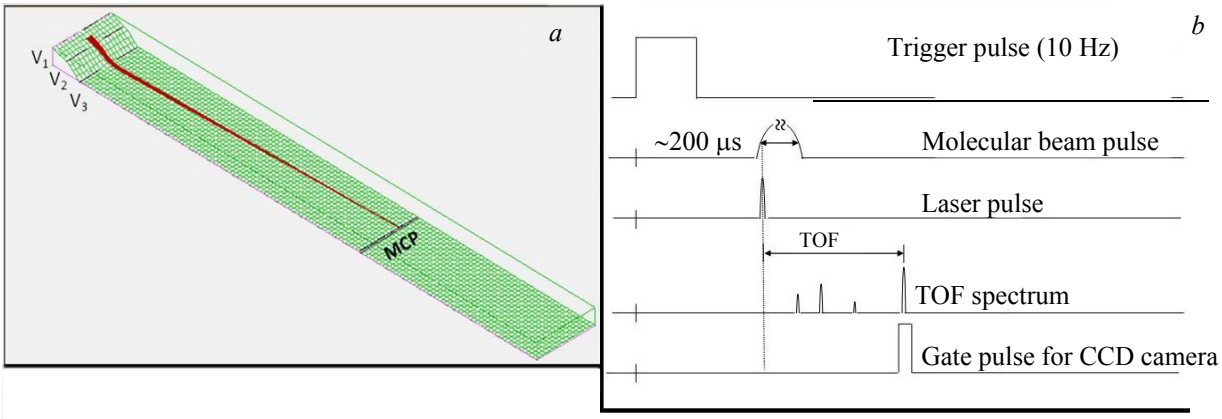

Fig. 1. a) Electric field simulation by SIMION (version 8, Scientific Instrument Services) program package. The lens is designed to focus ions with the same initial velocity in the same position on the detector; b) the timing diagram of the VMI setup. The laser pulse hits the early portion of the molecular beam to minimize the cluster dissociation.

with 0.8% of oxalyl bromide ($C_2O_2Br_2$), seeded in He at a stagnation pressure of ~2 atm after several freeze-pump-thaw cycles. To produce the molecular beam, the pulse valve was operated at 10 Hz with an opening time of 200 μs. A dye laser (Lumonics, HD500) pumped by a Quanta-Ray Nd:YAG laser (Spectra physics, Lab-150-10) was used to produce a 30–100 μJ/pulse at 10 Hz and subjected to focusing onto the rising edge of the molecular beam by a plano-convex lens with a focal length of 150 mm (Fig. 1b). The $C_2O_2Br_2$ was photolyzed by the UV laser light, and the resulting bromide atom fragments were then selectively ionized by the [2+1] REMPI technique: 264.9 and 233.69 nm for Br, and 264.8 and 234.03 nm for Br* [16].

Timing was controlled with respect to a source trigger (reference) for each laser shot. The reference signal was generated by a photodiode collecting scattered laser light in the input path before the laser was focused into the molecular beam. The velocity mapping signal from the detector at the end of the time-of-flight tube was integrated by a CCD camera. To avoid the undesirable signal from the microchannel plate-phosphor screen (MCP/PS) detector, the CCD camera was operated with a narrow pulse gate only. Each image was recorded for 10000 laser shots, and the background was removed by subtracting a reference image collected at an off-resonant wavelength under the same experimental conditions. All images and spectra were averaged over a range of ±0.04 cm^{-1} to cover all velocity components of the desired fragment ions. To acquire the REMPI time-of-flight (TOF) spectra, a photomultiplier tube (Hamamatsu, 1P21) was used instead of the CCD camera.

Results and discussion. The raw images corresponding to Br and Br* resulting from the photolysis of $C_2O_2Br_2$ at 265 and 234 nm are shown in Fig. 2. The acquired two-dimensional raw images are the projection of the 3-D velocity distribution with cylindrical symmetry around the laser polarization axis. The cylindrical symmetry of this velocity distribution profile allows us to reconstruct a 3-D image by performing the inverse Abel transformation [17]. The transformation process is very sensitive to noise, so all the images are pre-smoothed using a Gaussian filter, 5×5 window, with a standard deviation 2 in pixel units to reduce the noise effect [18]. Therefore, the constructed 3-D shape of the image contains all the information about the speed and angular distribution of the fragments.

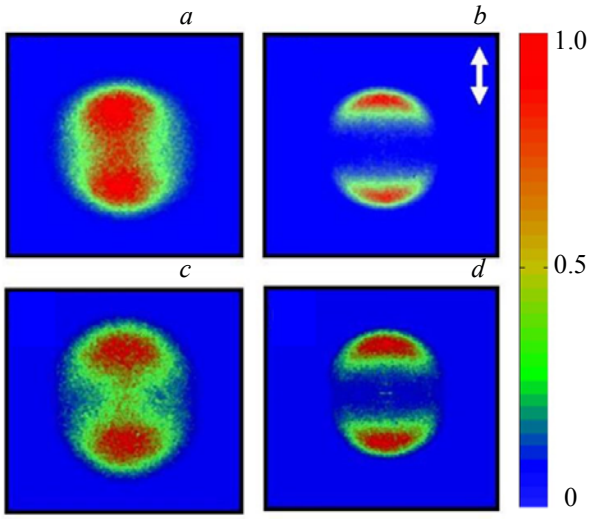

Fig. 2. Raw images of Br (a, c) and Br* (b, d) ions from the photolysis of $C_2O_2Br_2$ at 265 and 234 nm are shown along with the laser polarization axis (vertical arrow). The color coding is also indicated on the right.

The speed distribution can be extracted by integrating the reconstructed 3-D speed distributions over all angles at each speed. The center-of-mass translational energy distribution, $P(E)$, was obtained by the speed distribution using the following equations [19]:

$$P(E_T)dE = P(v)dv\,, \tag{1}$$

$$E_T = \frac{1}{2}(m_{\mathrm{Br}} + m_{\mathrm{C_2O_2Br}})\frac{m_{\mathrm{Br}}}{m_{\mathrm{C_2O_2Br}}}v_{\mathrm{Br}}^2\,, \tag{2}$$

where m and v stand for the mass and recoil velocity of the corresponding fragments, respectively.

The corresponding total translational energy, E_T, and the distribution with the anisotropy parameter, β [20], for Br and Br* at 265 and 234 nm are displayed in Fig. 3, and the E_T values of each velocity components are summarized in Table 1. The β values vary from 0–0.90(0–0.79) and 0–1.38(0–0.97) for Br and Br*, respectively, at 265(234) nm. The values, which deviate from the limiting values, may originate from different origins such as the long lifetime of the excited state, the secondary dissociation, and the deviation of the recoil axis from the transition dipole moment. It also can be mentioned that multiple channels contribute to the formation of Br and/or Br* in the photolysis of $C_2O_2Br_2$ at 265 and 234 nm. These findings can be clearly explained by the total translation energy distribution, which is characterized by several components.

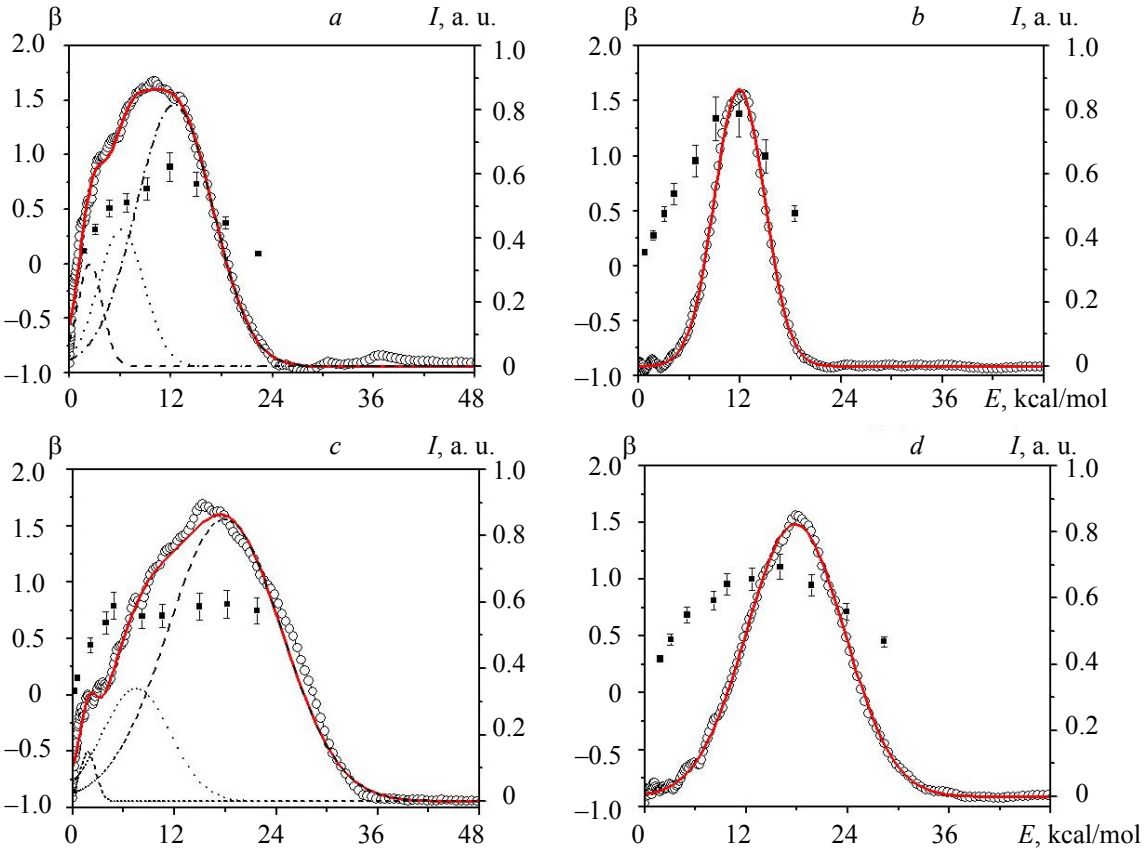

Fig. 3. Total translational energy distributions of Br($^2P_{3/2}$) (a, c) and Br*($^2P_{1/2}$) (b, d) from the photodissociation of $C_2O_2Br_2$ at 265 and 234 nm. Each data point (○) corresponds to the relative signal intensity obtained by the integrated values for all angular components at a specific translational energy. The anisotropy parameters (▪) are also displayed as a function of the translational energy. The right axis indicates the normalized counts of intensity. In all figures, the dashed lines, dotted lines and dash-dot lines correspond to the low, middle, and high Gaussian components, respectively. The linear combinations of the overall components are displayed as solid red lines.

The relative quantum yield for Br and Br* was determined from the relative peak intensity of the TOF spectra. The measured ion signal ratio is proportional to the product ratio by the k factor,

$$\frac{N(\mathrm{Br^*})}{N(\mathrm{Br})} = k\frac{I(\mathrm{Br^*})}{I(\mathrm{Br})}, \tag{3}$$

where $N(X)$ and $I(X)$ (X = Br and Br*) designate the number and the measured signal intensity of the species X, respectively. The proportional constant k depends strongly on the relative detection efficiency and the experimental conditions, and it was estimated to be 0.42 from the CCl_3Br photolysis under the same experimental condition [21]. From the calculated ratio, the relative quantum yield of each channel was determined by the following relationship:

$$\frac{N(\mathrm{Br}^*)}{N(\mathrm{Br})} = k\frac{S(\mathrm{Br}^*)}{S(\mathrm{Br})}, \tag{4}$$

The resultant quantum yields for Br* are 0.42 and 0.33 at 265 and 234 nm, respectively. Using these values, the relative quantum yields for each energy components in Fig. 3 are also extracted and listed in Table 2. The relative quantum yield of Br*, 0.33, at 234 nm is very close to the measured quantum yield of Cl*, 0.36, in the photodissociation of $C_2O_2Cl_2$ at 235 nm [6].

TABLE 1. The Average Energy Values for Each Translational Energy (in kcal/mol) Component of Br/Br* Formation Channels at 265 and 234 nm

Channel	$h\nu$	E_{avl}	E_T^{low}	E_T^{middle}	E_T^{high}
$C_2O_2Br + Br$	107.79	48.26	2.34	6.10	12.49
$C_2O_2Br + Br^*$		37.75	–	–	11.9
$C_2O_2Br + Br$	107.79	48.26	2.34	6.10	12.49
$C_2O_2Br + Br^*$		37.75	–	–	11.9

TABLE 2. The Relative Quantum Yields for Each Translational Energy Component of Br/Br* Formation Channels at 265 and 234 nm

Channel	$h\nu$	Φ^{low}	Φ^{middle}	Φ^{high}	Φ^{total}
$C_2O_2Br + Br$	107.79	0.05	0.13	0.40	0.58
$C_2O_2Br + Br^*$		–	–	0.42	0.42
$C_2O_2Br + Br$	107.79	0.01	0.13	0.53	0.67
$C_2O_2Br + Br^*$		–	–	0.33	0.33

The features of Br* images are qualitatively different from those of Br, which are shown in Fig. 2. In Fig. 3, the corresponding translational energy distribution of Br* is well fitted by the single Gaussian functions with the high β value of 1.38(0.97) at 265(234) nm. The average recoil energy of this component is measured to be 11.9 kcal/mol at 265 nm and 17.84 kcal/mol at 234 nm. On the other hand, the corresponding translational energy distributions of Br images are quite different and fitted with three Gaussian functions at both pump sources, indicating that at least three different reaction pathways contributed in the formation of the Br image. The relative oscillator strengths of different electronic transition and associated coupling dynamics between the three accessible states (n,π^*), (π,σ^*), and (n,π^*) are not discussed in the text, because our main aim is to focus on the photo-induced stepwise multi-body dissociation process. In order to infer the reaction pathways, the energetics involved in the following reaction needs to be considered.

$$C_2O_2Br_2 + h\nu \rightarrow {}^{\bullet}C_2O_2Br + Br/Br^* \tag{5}$$

$${}^{\bullet}C_2O_2Br \rightarrow C_2O_2 + Br \tag{6}$$

The first step (Eq. (5)) is the direct C-Br bond dissociation after one photon absorption, and the second step (Eq. (6)) is the secondary dissociation of the internally excited C_2O_2Br fragments. According to the theoretical study of oxalyl bromide [22], the first excited state (S_1) of $C_2O_2Br_2$ has two equivalent C–Br bonds in the *trans* direction and the C–Br bond dissociation energy is 59.53 kcal/mol. The secondary dissociation of the C_2O_2Br radical at the ground state was also observed in the calculation, where the C–C and C–Br bond dissociation of the C_2O_2Br radical occurred synchronously with a barrier of 5.43 kcal/mol. Considering this relatively small energy barrier (5.43 kcal/mol), as only a small portion of the internal energy participates in the recoil direction due to the randomization of energy prior to the bond breaking, the secondary dissociation of the C_2O_2Br radical should be countable. The available energies for the primary photolysis are 48.26(62.84) and 37.75(52.33) kcal/mol for the Br and Br* elimination at 265(234) nm (see Table 1). The corresponding internal energies of the C_2O_2Br radicals produced via two pathways are estimated to be 35.77(45) and 25.85(34.49) kcal/mol, respectively. The C_2O_2Br radicals with sufficient energy, which are attributed via two pathways at both excitation wavelengths, are responsible for Br. The contribution of the Br

fragment via decomposition of the C_2O_2Br radical, however, is more pronounced at 265 nm. This is partly due to the narrower energy distribution of the primary products at the pump energy of 265 nm compared to that at 234 nm, as clearly observed in the Br (high velocity component) and Br* translational energy distribution at both excitation wavelengths. Considering the different origin of C_2O_2Br via $C_2O_2Br + Br$ and $C_2O_2Br + Br^*$ pathways, two additional distinguishable velocity components, the Gaussian-shaped components with peaks at ~7 kcal/mol (middle velocity component) and ~2 kcal/mol (low velocity component), appeared in the Br formation process.

The secondary C-Br bond dissociation was observed in the photodissociation of 1,2-dibromopropane at 265 and 234 nm [23], in which the secondary C-Br bond cleavage of bromopropyl radicals with different internal energies from the Br/Br* elimination pathways is attributed to the middle and low kinetic energy profiles. Similar results were also observed in the photodissociation of Cl_2O at 235 nm, except for the absence of the low velocity component [24]. This difference might be due to the four times larger spin-orbit coupling energy of Br (10.5 kcal/mol) than that of Cl (2.51 kcal/mol). Therefore, the Cl fragment from ClO radicals, resulting from both Cl and Cl* elimination pathways, generates only one translational energy profile. It might be argued that the Br fragment may be attributed to the dissociation of the primary Br_2 photo product, but the relatively high dissociation energy of Br_2 (45.89 kcal/mol) refutes this possibility [13]. The multiphoton process, however, may need to be considered in order to find out whether it is a single-photon process or not. The translational energy of Br fragments can be estimated by the following equation:

$$E_T(\mathrm{Br}) = \frac{m_{\mathrm{Br}}}{m_{\mathrm{Br_2}}}\left\{E_{h\nu} + E_{\mathrm{int}}(\mathrm{Br_2}) - D_0(\mathrm{Br\text{-}Br}) - E_{el}(\mathrm{Br})\right\}, \quad (7)$$

where $E_{h\nu}$ is the photon energy, 107.79 kcal/mol for 265 nm and 122.37 kcal/mol for 234 nm. The dissociation energy D_0(Br-Br), electronic energy E_{el}, and internal energy $E_{\mathrm{int}}(Br_2)$ are available in the literature [13]. In the two-photon dissociation process, the translational energies of Br could be 37.64 and 44.93 kcal/mol at 265 and 234 nm, respectively. However, no signature appeared corresponding to these values. Moreover, we performed the excitation laser power dependent experiment. The linear dependence of the Br formation with the laser fluence confirmed that the single photon was only involved in all Br formation channels.

To deconvolute the nature of the translation energy distribution of Br images, we also measured the angular distribution of each component. The recoil anisotropy parameter, β, and values of Br* are measured to be 1.38 and 1.07 at 265 and 234 nm, respectively. The higher β values of Br* image suggest that the product state distribution is diabatically correlated with the excited state, where the transition dipole moment is parallel to the C-Br bond axis at both excitation energies. In contrast, the angular distribution of the Br image is quite interesting for its peanut-shaped structure. The spherical-shape splitting along the laser polarization direction implies that the secondary Br fragment may be isotropic. The initial transverse velocity imparted to the C_2O_2Br radical is responsible for the underlying peanut-shaped vertical anisotropic distribution. The isotropic angular distribution for the secondary Br fragment is more pronounced at 265 nm compared with that at 234 nm. This is particularly due to the slow secondary dissociation rate at the low internal energy of the C_2O_2Br radical generated at 265 nm. The isotropic distribution in both Br images implies that the secondary C-Br bond dissociation occurs at the ground state. Furthermore, in a single color, experiment, the Br fragment from the secondary C-Br bond cleavage should appear in the image only when the pertinent dissociation event occurs within the laser pulse width (3–5 ns). In other words, the laser beam cannot ionize the Br fragment, which appears in the interaction region behind the laser pulse. Considering the time constant of the sequential secondary dissociation or the spontaneous secondary dissociation (dissociation occurs within the vibrational time period) for intermediates, the laser pulse width (3–5 ns) may be long enough to cover most of the fragments except those being generated near the reaction threshold. A similar phenomenon was also observed in the calculation results performed by Geng et al. [22]. In their observation the C_2O_2Br radicals with high internal energy are prone to release into the ground state, and sequentially decompose into Br + 2CO with a 3.49 kcal/mol kinetic energy release. In such a sub-sequential process, the observed β value of the secondary Br fragments will deviate from the exact angular distribution of this channel because the final angular distribution of a fragment is dynamically linked to the product of each dissociation step.

Conclusions. In this work, we have used the velocity map ion imaging technique coupled with a state selective [2+1] REMPI scheme. To obtain the detail dynamics, the translational energy distribution and recoil anisotropy of the Br(^2P_J, $J = 3/2, 1/2$) atom formation process are extracted from the acquired two-dimensional ion images. The nascent Br($^2P_{1/2}$) atoms stem from the primary C–Br bond, whereas, the Br($^2P_{3/2}$) atoms are attributed to the primary C–Br bond fission as well as the secondary dissociation of their

corresponding C_2O_2Br radicals, which are energized from the ultrafast primary photodissociation steps at both pump energies. On the basis of the proposed mechanism in the formation of each component of $Br(^2P_{3/2})$, the ultrafast primary one of the C–Br bond dissociation of $C_2O_2Br_2$ is responsible for the high velocity component, and the subsequent secondary dissociation of C_2O_2Br radicals (from primary Br and Br* pathways) is responsible for the middle and low velocity components, respectively.

Acknowledgements. This work was supported by the Basic Science Research Program 2010-0006570 through the National Research Foundation of Korea (NRF) funded by the Ministry of Education, Science, and Technology.

REFERENCES

1. C. Escure, T. Leininger, B. Lepetit, *J. Chem. Phys.*, **130**, 244305(1–10) (2009).
2. V. Blanchet, P. C. Samartzis, A. M. Wodtke, *J. Chem. Phys.*, **130**, 034304(1–11) (2009).
3. C. Hu, S. Pei, Y.-L. Chen, K. Liu, *J. Phys. Chem. A*, **111**, 6813–6821 (2007).
4. Y. Amatatsu, K. Morokuma, S. Yabushita, *J. Chem. Phys.*, **94**, 4858–4876 (1991).
5. E. M. Warne, B. D.-Ward, J. Woodhouse, M. A. Parkes, D. Bellshaw, E. Springate, P. Majchrzak, Y. Zhang, G. Karras, A. S. Wyatt, R. T. Chapman, A. Kirrander, R. S. Minns, *Phys. Chem. Chem. Phys.*, **21**, 11142–11149 (2019)
6. M. Ahmed, D. Blunt, D. Chen, A. G. Suits, *J. Chem. Phys.*, **106**, 7617–7624 (1997).
7. N. Hemmi, A. G. Suits, *J. Phys. Chem. A*, **101**, 6633–6637 (1997).
8. B. Ghosh, D. K. Papanastasiou, J. B. Burkholder, *J. Chem. Phys.*, **137**, 164315(1–12) (2012).
9. Q. Fang, L. Shen, W.-H. Fang, *J. Chem. Phys.*, **139**, 024310(1–10) (2013).
10. C. Y. Wu, Y. P. Lee, J. F. Ogilvie, N. S. Wang, *J. Phys. Chem. A*, **107**, 2389–2393 (2003).
11. Q. Fang, Mechanistic Photodissociation of Small Molecules Explored by Electronic Structure Calculation and Dynamics Simulation, KTH Royal Institute of Technology (2011).
12. T.-K. Huang, B.-J. Chen, K.-C. Lin, L. Lin, B.-J. Sun, A. H. H. Chang. *Phys. Chem. A*, **121**, 2888–2895 (2017).
13. C.-C. Wu, H.-C. Lin, Y.-B. Chang, P.-Y. Tsai, Y.-Y. Yeh, H. Fan, K.-C. Lin, J. S. Francisco, *J. Chem. Phys.*, **135**, 234308(1–9) (2011).
14. J. E. Tuttle, G. K. Rollefson, *J. Am. Chem. Soc.*, **63**, 1525–1530 (1941).
15. A. T. J. B. Eppink, D. H. Parker, *Rev. Sci. Intrum.*, **68**, 3477–3484 (1997).
16. M. S. Park, Y.-J. Jung, S.-H. Lee, D.-C. Kim, K.-H. Jung, *Chem. Phys. Lett*., **322**, 429–438 (2000).
17. S. M. Candel, *IEEE Trans. Acoust. Speech Signal Process.*, **29**, 963–972 (1981).
18. E. W. Hansen, P.-L. Law, *J. Opt. Soc. Am. A*, **2**, 510–520 (1985).
19. T. K. Kim, M. S. Park, K. W. Lee, K.-H. Jung, *J. Chem. Phys.*, **115**, 10745–10752 (2001).
20. R. N. Zare, *Mol. Photochem*., **4**, 1–37 (1972).
21. Y.-J. Jung, M. S. Park, Y. S. Kim, K.-H. Jung, *J. Chem. Phys.*, **111**, 4005–4012 (1999).
22. Z.-Y. Geng, D.-M. Wang, Y.-C. Wang, G.-L. Dai, L.-L. Lu, H.-Q. Wang, *Chin. J. Struct. Chem.*, **24**, 1334–1339 (2005).
23. K.-S. Lee, K. Y. Yeon, K.-H. Jung, S. K. Kim, *J. Phys. Chem. A*, **112**, 9312–9317 (2008).
24. H. Kim, S. M. North, *J. Photochem. Photobiol. A: Chem.*, **221**, 123–127 (2011).